MATERIALS CHEMISTRY
FRONTIERS

RESEARCH ARTICLE

View Article Online
View Journal

Check for updates

Cite this: DOI: 10.1039/d6qm00202a

Biodegradable single-electrode triboelectric nanogenerator for self-powered robotic texture sensing

Sugato Hajra,[a] Shibam Pal,[b] Kushal Ruthvik Kaja,[a] Yoobin Choi,[a] Swati Panda,[a] Basanta Kumar Panigrahi,[c] Hoe Joon Kim *[a] and Anna Finne Wistrand *[b]

Human tactile acuity relies on the microstructured morphology of the fingertips, which enables sensitive detection of fine surface features during object manipulation. While triboelectric-based self-powered object recognition has gained much attention, conventional triboelectric materials are typically non-biodegradable, contributing to persistent electronic waste. This work focuses on fabricating biodegradable triboelectric interfaces for intelligent robotic texture perception and sustainable energy harvesting. Three biodegradable polymers, polylactide (PLA), poly(ε-caprolactone) (PCL), and poly(lactide-*co*-trimethylene carbonate) (PTMC), were evaluated as negative triboelectric layers against an aluminum electrode to form a single-electrode triboelectric nanogenerator (TENG). The PCL/Al TENG achieved a superior electrical output of 118 V and 772 nA, with a peak power of 24.5 μW at 200 MΩ, primarily due to its higher surface roughness enhancing charge transfer. The powering of the low-power electronics and charging of the capacitors using the TENG was demonstrated. In addition, the platform was integrated into a robotic gripper for real-time texture recognition. Combined with a convolutional neural network (CNN), the system achieved 96.9% classification accuracy across eight distinct textures. This sustainable platform reduces environmental impact by using degradable materials while maintaining the mechanical robustness required for advanced robotic sensing.

Received 17th March 2026,
Accepted 11th May 2026

DOI: 10.1039/d6qm00202a

rsc.li/frontiers-materials

Open Access Article. Published on 14 May 2026. Downloaded on 6/5/2026 3:58:04 AM.
This article is licensed under a Creative Commons Attribution 3.0 Unported Licence.

1. Introduction

Intelligent automation has transformed manufacturing environments, with robotic grippers at the heart of modern pick-and-place systems.[1,2] Traditional surface-texture sensors used in robotic grippers, such as resistive or capacitive types, respond primarily to static pressure and require constant external power, making large-scale integration difficult and energy-intensive.[3–5] Their sensitivity to micro-scale frictional fluctuations and high-frequency vibrations is often limited, making them less useful for detecting subtle texture differences or early slide events.[6] Self-powered sensing technologies offer an effective alternative by eliminating the need for external power sources.[7] Depending on their operating principles, sensors incorporated into robotic systems can generally be categorized as resistive, capacitive, piezoelectric, triboelectric, and optical types.[8,9] Among these, TENGs stand out because they can serve dual roles: functioning both as energy harvesters to power soft robotic systems and act as active sensing elements.[10–12] TENG operates in four working modes: vertical contact separation, lateral sliding, free-standing, and single-electrode mode. TENG-based sensing devices are commonly fabricated from flexible polymers and elastomeric materials, which makes them highly compatible with robotic systems. In addition, the electrical outputs from TENGs exhibit strong sensitivity to mechanical stimuli, producing clear, distinguishable signals. In single-electrode mode, only one active electrode is required, with the object itself serving as the counter electrode, making the device more flexible, and adaptable to arbitrary contact, which is essential for real-world tactile interactions where the contacting material, shape, and grounding conditions can vary. In contrast, a two-electrode contact–separation TENG requires two predefined friction layers and controlled alignment, limiting direct exposure of the sensing surface and reducing sensitivity to external touch stimuli. These characteristics make TENG-driven self-powered sensors highly attractive for practical integration into next-generation soft robotic systems.

One of the most notable advantages of TENGs is their ability to transform readily available mechanical energy, such as

[a] Department of Robotics and Mechatronics Engineering, Daegu Gyeongbuk Institute of Science and Technology, Daegu 42988, Republic of Korea. E-mail: joonkim@dgist.ac.kr
[b] Department of Fibre and Polymer Technology, KTH Royal Institute of Technology, Stockholm 11428, Sweden. E-mail: annaf@kth.se
[c] Department of Electrical Engineering, Siksha O Anusandhan University, Bhubaneswar-751030, India

Open Access Article. Published on 14 May 2026. Downloaded on 6/5/2026 3:58:04 AM. This article is licensed under a Creative Commons Attribution 3.0 Unported Licence.

airflow, water movement, body motion, and ambient vibrations, into useful electrical power.[13–16] Because of these capabilities, TENG technology has been investigated in a wide range of domains, including IoT systems, AI and ML-enabled platforms, agricultural monitoring, healthcare devices, smart home technologies, and wearable electronics.[17–21] In addition to energy harvesting, TENGs can serve as flexible, self-powered sensing devices, broadening their functionality.[22] Their remarkable responsiveness to mechanical stimuli and adjustable structural design make them ideal for tactile sensing in robot grippers.[23] However, a variety of gripper configurations rely on passive grasping due to the increased complexity of incorporating conventional sensors, which require wiring and a specific power supply.[24,25] Flexible TENG-based sensors, on the other hand, offer a promising path to more streamlined and adaptable gripper systems by reducing wiring requirements and enabling seamless integration with a wide range of gripper layouts.

Biobased materials such as cellulose, chitosan, lignin, and gelatin, as well as biodegradable synthetic polymers like PLA and polyvinyl alcohol (PVA), have been extensively studied as triboelectric components in TENG systems.[26,27] Despite these developments, significant research gaps remain in eco-friendly TENGs. Most research has focused on biodegradable materials that act as positive triboelectric layers, but efficient degradable compounds suitable for the negative triboelectric layer remain few.[28] Many ''environmentally friendly'' TENGs continue to use polymers such as fluorinated ethylene propylene (FEP), polydimethylsiloxane (PDMS), and polytetrafluoroethylene (PTFE) as the negative layer due to their high electron affinity, stable charge storage, and durability.[28–30] However, these compounds persist in the environment after disposal, hindering progress towards sustainability objectives. Pei *et al.* demonstrates a sustainable strategy using biomass-derived melanin-like nanoparticles to simultaneously enhance mechanical durability, phase compatibility, and triboelectric performance in biodegradable polymer blends. It enables the development of stable, high-performance (up to 414.88 μC m^{-2}) and eco-friendly wearable TENGs for reliable human motion sensing and energy harvesting.[31] Kan *et al.* focus on enhancing TENG performance by incorporating dipolar cellulose nanoparticles into PVDF-HFP nanofibrous membranes to increase the dielectric constant and interfacial charge generation with TPU. This results in significantly improved electrical output, achieving high voltage (281.5 V), current density, transferred charge, and a power density of 5.92 W m^{-2} with excellent operational stability.[32]

Growing interest in sustainable technology has encouraged the use of low-cost biomass resources rich in natural polymers and surface roughness beneficial for triboelectrification. Although biodegradable polymers have been explored for applications in packaging, sensing, and healthcare materials, their direct use in energy harvesting remains limited.[33,34] A wide range of sustainable materials, such as cellulose, chitin, and silk fibroin, have demonstrated biodegradability, biocompatibility, and suitable triboelectric behavior for the development of eco-friendly TENGs.[26] Subsequent research has introduced implantable biodegradable TENGs made from layered combinations of absorbable metals and polymers, such as PLGA, PCL, and PVA, which are inexpensive, readily available, and easy to prepare.[35] The electrical output may be controlled by selecting materials based on their electron-donating or electron-accepting tendencies, yielding voltages ranging from 10 to 40 V under laboratory conditions.[36–38] These devices can be safely decomposed and absorbed *in vivo* after they have served their purpose, and their total breakdown rate can be controlled using specific encapsulating materials. Hence, in terms of negative polarity, biodegradable triboelectric materials will extend the conventional triboelectric series and enhance the design of TENG applications. Table S1 compares the performance of the TENG based on biocompatible materials with that of the present work.

This work explores biodegradable polymers as functional triboelectric materials in a single-electrode mode TENG design. The polymers and metals currently in the triboelectric series are non-biodegradable and end up in landfills after use. Hence, biodegradable polymers are necessary not only as alternatives to triboelectric layers but also as materials that can be degraded after TENG fabrication or application. The device was optimized using a biodegradable negative layer paired with aluminum as the positive triboelectric counterpart, demonstrating stable, reliable electrical output. Practical demonstrations included charging a capacitor and powering a calculator. The TENG was further integrated onto a robotic gripper for surface texture sensing. Coupled with a neural network, the system enabled intelligent tactile classification, highlighting its potential for scalable, sustainable robotics and human–machine interaction.

2. Materials and methods

PLA and PTMC were synthesized *via* ring-opening polymerization according to earlier published methods,[38] and PCL was purchased from Sigma-Aldrich (synthesis grade, Darmstadt, Germany). The single-electrode TENG was constructed by integrating a composite layer (biodegradable polymers such as PLA, PCL, and PTMC) onto a double-sided aluminum tape, with the composite serving as the tribonegative surface and the aluminum acting as the current-collecting electrode. The device was designed with an active area of 3 × 3 cm^2. A copper wire was connected to the aluminum electrode to transfer the induced charges during operation efficiently. A flexible PET backing layer was attached to the rear of the aluminum electrode to enhance mechanical support and durability.

The surface morphology of the polymer samples was examined using a field-emission scanning electron microscope (SU-8230, Hitachi, Japan) equipped with energy-dispersive X-ray spectroscopy (EDS) to determine their elemental composition. Crystalline characteristics were analyzed by powder X-ray diffraction (Malvern PANalytical Empyrean) using Cu-Kα radiation at a scan rate of 3° per minute. Surface topography and roughness parameters were evaluated using an atomic force microscope (Park Systems NX10, South Korea) fitted with a

 This journal is © The Royal Society of Chemistry and the Chinese Chemical Society 2026

Open Access Article. Published on 14 May 2026. Downloaded on 6/5/2026 3:58:04 AM.
This article is licensed under a Creative Commons Attribution 3.0 Unported Licence.

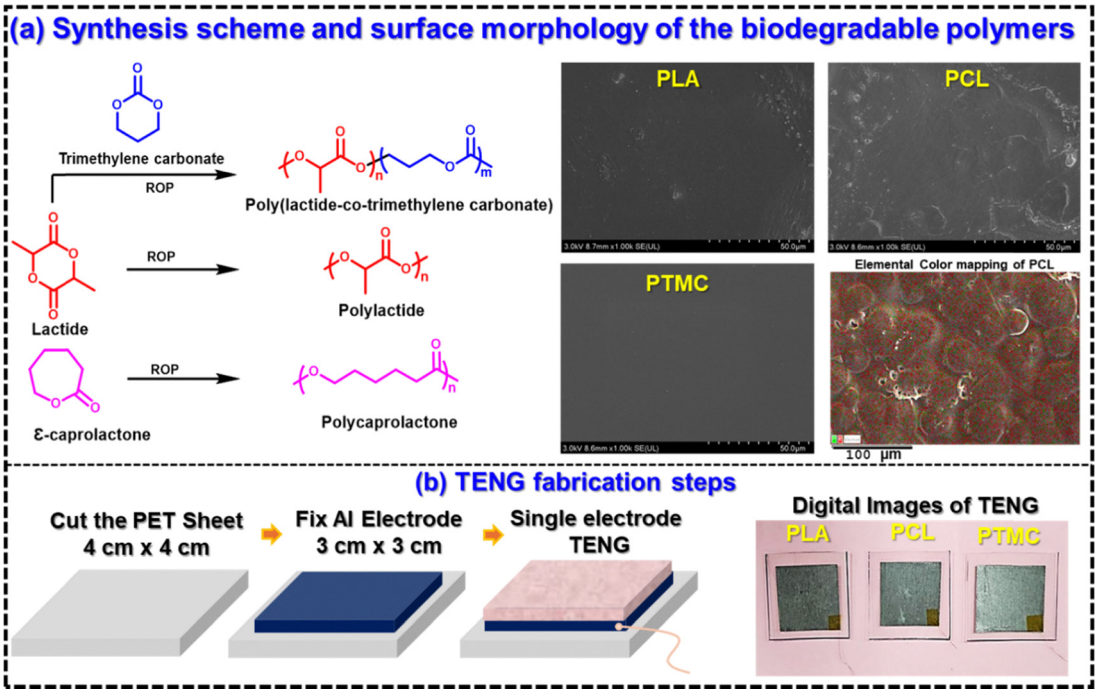

Fig. 1 (a) Synthesis scheme and surface morphology of the biodegradable polymers such as PLA, PCL, and PTMC, along with elemental color mapping of PCL, and (b) fabrication process of the triboelectric nanogenerator, along with a digital picture of the fabricated TENG.

PPP-NCHR probe. Structural characterization was further performed using a 400 MHz Bruker Avance Ultrashield NMR spectrometer, with CDCl3 with TMS as the solvent for the NMR measurements. Thermal analysis behavior was assessed using a Mettler-Toledo DSC3+ under a nitrogen flow of 50 mL min^{-1}.

Samples weighing approximately 10 mg were subjected to a heating–cooling–heating cycle. For PLA and PTMC, the temperature range was from −30 to 180 °C at a heating rate of 10 K min^{-1}. For PCL, the temperature range was 0 to 125 °C at a constant heating rate. The molecular weight of the polymers was determined by size-exclusion chromatography (SEC) using chloroform as the eluent. The analysis was carried out on a Malvern GPC Max system equipped with a PL gel 5 µm guard column (7.5 × 50 mm) and a refractive index (RI) detector. HPLC-grade chloroform was used as the mobile phase, and the column temperature was maintained at 35 °C. Polymer samples were prepared at a concentration of 3 mg mL^{-1}. The injection volume was 100 µL, and the flow rate was set to 0.5 mL min^{-1}. The electrical performance of the TENG device was recorded using a Keithley 6514 electrometer connected to a computer running LabVIEW software for real-time data acquisition. Controlled periodic mechanical excitation was applied using a LinMot linear motor (USA).

3. Results and discussion

Fig. 1a shows the synthesis scheme and surface morphology of the biodegradable polymers, PCL, PLA, and PTMC. The molecular weights of PLA, PCL, and PTMC are 102, 154, and 354 kg mol^{-1}, respectively. PLA has a rigid, semicrystalline polyester structure due to its methyl side groups, while PCL, derived from ε-caprolactone, is flexible and ductile, with long aliphatic chains that enhance chain mobility. Because of these structural differences, PCL has the highest crystallinity and the lowest melting point. PTMC, derived from trimethylene carbonate, is amorphous, highly flexible, and has a low glass transition temperature. The surface morphology of PLA is relatively smooth and dense, with minimal surface irregularities, whereas PCL exhibits noticeable surface texture and microstructural features, suggesting higher surface roughness. PTMC exhibits highly uniform, smooth morphology, indicating amorphous characteristics and homogeneous film formation. The elemental color map of the PCL sample shows the presence of C and O, consistent with the base composition, with no impurities. Fig. 1b depicts the step-by-step fabrication process for a TENG and its digital image. A conductive substrate, such as aluminum foil, is prepared as the current collector. The substrate was collected from waste packaging PET. Then, double-sided aluminum (Al) electrode tape was attached to it, and the active area was defined as 3 cm × 3 cm. The biodegradable polymer film (PLA, PCL, or PTMC) was considered the tribonegative layer, while the free-moving Al layer was considered the tribopositive layer. Conductive wiring was integrated into the Al electrode for charge collection. The fabricated TENG operates in single-electrode mode.

Fig. 2a reveals the X-ray diffraction (XRD) differences in the crystalline structure of PLA, PCL, and PTMC. PLA displays a wide diffraction halo, centered and lacking distinct sharp reflections, confirming its predominantly amorphous nature.

Open Access Article. Published on 14 May 2026. Downloaded on 6/5/2026 3:58:04 AM.
This article is licensed under a Creative Commons Attribution 3.0 Unported Licence.

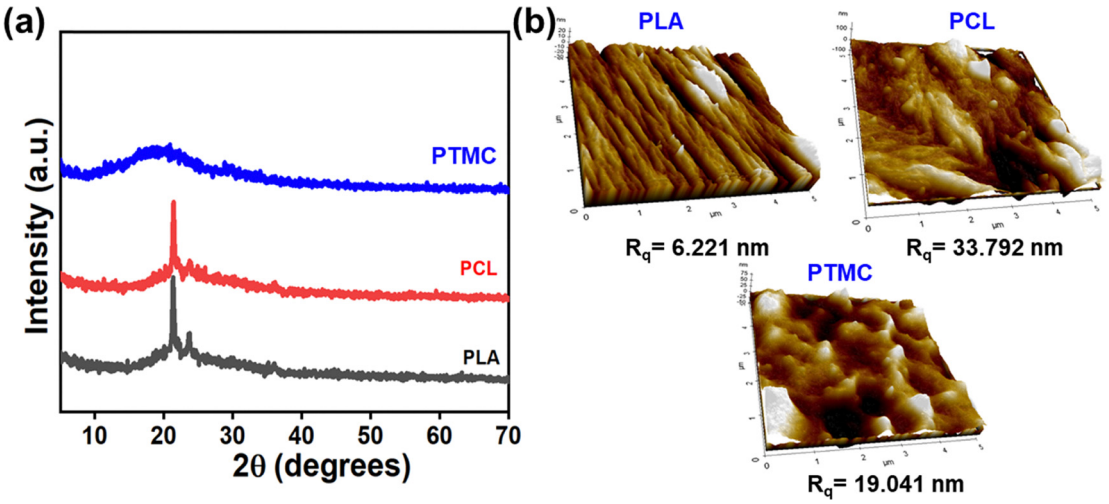

Fig. 2 (a) XRD spectra of biodegradable polymers, and (b) AFM morphology and roughness parameters of biodegradable polymers.

Distinct diffraction peaks for PCL appear near 21.5° and 23.8°, with minor positional shifts observed across the recorded patterns. These peaks correspond to the (110) and (200) lattice planes characteristic of the orthorhombic crystalline phase of polycaprolactone, confirming its semicrystalline structure. PTMC shows a board confirming a predominantly amorphous structure. The surface roughness and topography of the various polymers, as determined from AFM images, are shown in Fig. 2b. The surface roughness values (R_q) for PLA, PCL, and PTMC are 6.221 nm, 33.792 nm, and 19.041 nm, respectively. PCL exhibits higher R_q, increasing the effective contact area during triboelectric interaction. Higher surface roughness increases the effective contact area, promotes charge trapping, and improves mechanical interfacial interaction, collectively leading to higher voltage, current, and charge output in biodegradable polymer-based TENG devices. The characterization of the polymers was performed using NMR (Fig. S1), SEC, and DSC (Table S2).

PLA, PCL, and PTMC exhibit distinct thermal and crystalline properties. PLA has a relatively high glass transition temperature (T_g) of 40 °C, a high melting temperature (T_m) of 155 °C, and a crystallinity of 26%, indicating a material that is fairly rigid at room temperature and moderately crystalline. In contrast, PCL has a much lower T_g, meaning it remains flexible at lower temperatures, and a significantly lower T_m of 56 °C. However, its crystallinity is 65%, suggesting a highly ordered structure that can contribute to toughness and slow degradation.[39] PTMC, on the other hand, has a T_g of 27 °C, which is lower than PLA but higher than PCL, and a Tm of 164 °C. Despite this high melting temperature, its crystallinity is only 3.4%, making it far more amorphous than both PLA and PCL. Overall, PLA appears semicrystalline; PCL is the most crystalline and most flexible; and PTMC combines a relatively moderate T_g with the highest melting point and the lowest crystallinity, highlighting major differences in their molecular organization and thermal performance.

Fig. S2 shows the room temperature dielectric constant for three polymers, such as PLA, PCL, and PTMC, at various frequency sweeps. All the polymers show typical dielectric behavior. In this context, the dielectric constant was observed to be high at low frequencies, while it decreased at high frequencies. It is because at low frequency all the polarization is activated, while at higher frequency, due to the rapidly changing electrical field, the dipoles cannot follow it, leading to a decrease in the dielectric constant. At 10 kHz, the dielectric constants of PLA, PCL, and PTMC are 2.99, 3.4, and 2.7, respectively. After 7 days of degradation, the PCL films exhibited approximately 45% weight loss, as shown in Fig. S3. The degradation study was conducted in a highly concentrated NaOH solution (5 M) to accelerate the process, promoting surface erosion through hydrolytic cleavage of the ester bonds present in the PCL matrix. As degradation progressed, noticeable changes in the film morphology were observed. The surface became increasingly rough, and in some cases, visible cracks developed, indicating structural weakening caused by surface polymer chain scission. This behavior suggests that degradation predominantly occurs *via* surface erosion under these conditions. Although PCL is known to degrade very slowly under normal environmental conditions, this accelerated study demonstrates its inherent susceptibility to hydrolytic degradation. Therefore, the results confirm the degradability of PCL films in alkaline environments and provide insight into their long-term behavior under extreme conditions.

Fig. 3a illustrates the operating principle of the triboelectric nanogenerator in single-electrode contact–separation mode. When the two triboelectric layers come into physical contact, charge transfer occurs due to differences in their electron affinity. The tribonegative layer gains electrons, while the tribopositive layer becomes positively charged. An electric potential difference arises from a charge imbalance, inducing electron flow from the ground to the electrode to balance the electrostatic field. This creates a positive peak in the electrical signal at maximum potential difference when the layers are fully apart, and equilibrium is established. As the layers move toward each other again, electrons flow in the opposite

 This journal is © The Royal Society of Chemistry and the Chinese Chemical Society 2026

Open Access Article. Published on 14 May 2026. Downloaded on 6/5/2026 3:58:04 AM.
This article is licensed under a Creative Commons Attribution 3.0 Unported Licence.

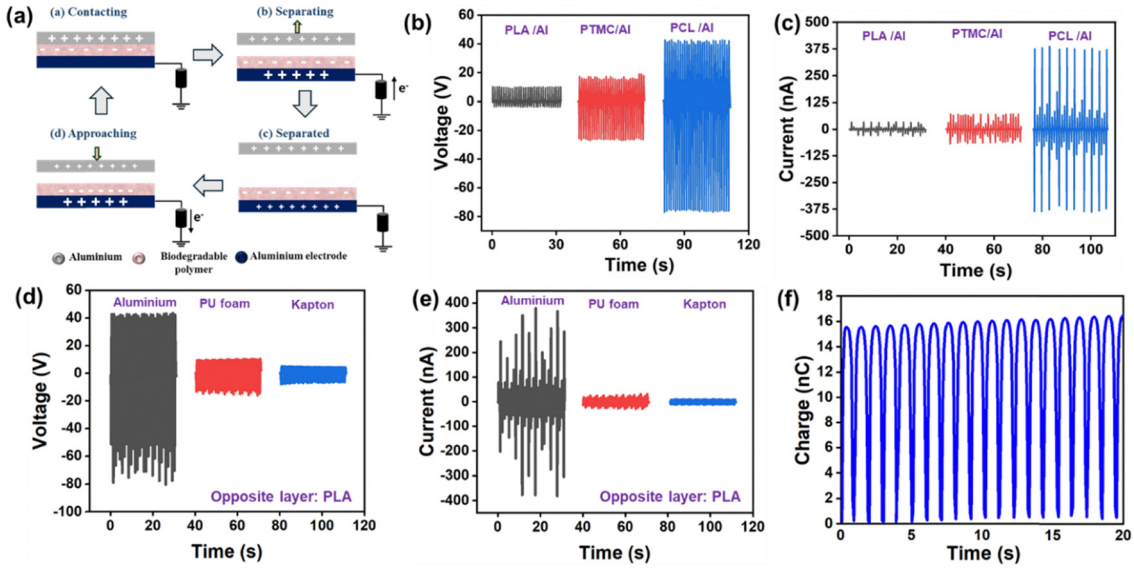

Fig. 3 (a) Schematic illustration of the working mechanism of the single electrode mode TENG, (b) output voltage signals obtained from devices fabricated with PLA/Al, PTMC/Al, and PCL/Al, (c) corresponding output current responses of PLA/Al, PTMC/Al, and PCL/Al devices, (d) output voltage TENG using a fixed PLA triboelectric layer with different counter triboelectric materials (aluminum, PU foam, and Kapton), (e) corresponding current outputs for TENG having PLA and different counter materials, (f) charge transfer characteristics of the optimized device demonstrate stable and repetitive charge generation under cyclic mechanical input.

direction, generating the negative peak of the electrical signal. This process of periodic contact and separation of the freely moving Al layer on the biodegradable polymer triboelectric layer generates a peak-to-peak electrical output signal.

Fig. 3b and c show the voltage and current responses of the biodegradable polymer-based TENG with the opposite free-moving layer fixed to Al. The electrical signals of the PLA/Al (13 V, 65 nA), PTMC/Al (42 V, 143 nA), and PCL/Al (118 V, 772 nA) were traced, confirming that the highest output was obtained from the PCL/Al TENG. The output also benefits from the roughness of the PCL films, which is higher than that of other biodegradable polymers such as PLA and PTMC, leading to greater charge generation. The electrical output of the biodegradable polymer-based TENG was evaluated with various triboelectric materials, including Al, PU foam, and Kapton, as shown in Fig. 3b and c. By boosting the surface charge density and enhancing charge retention during the contact–separation process, the Al counter layer improves device performance. As biodegradable polymers such as PCL, PTMC, and PLA act as a negative triboelectric layer, Al is more electropositive than PU foam and Kapton, resulting in higher electrical output in Fig. 3d and e. The superior performance of PCL/Al TENG arises mainly from its strong triboelectric polarity, as aluminum lies much higher in the triboelectric series than PU foam and Kapton, so it donates electrons more readily, generating a larger charge density during the impact process. The charge generated by the contact of Al with the PCL layer of TENG is 15 nC, as shown in Fig. 3f.

Fig. 4a and b show the frequency-dependent voltage and current response of the PCL/Al-based TENG. To further optimize device performance, the influence of operating frequency on the TENG output was systematically examined by varying it from 0.3 to 2 Hz. The voltage output of the PCL/Al TENG is almost constant as the charge generated by both layers of TENG remains constant. However, in the current case, as the frequency rises, the flow of electrons through the load resistance increases. At lower frequencies, relatively lower current output is observed because the slower contact–separation motion limits the rate of charge transfer. As the frequency increases, more rapid mechanical cycling enhances electrostatic induction, leading to a maximum current output. The improved current output at higher frequencies is attributed to increased contact events per second, which accelerate surface charge generation and electrostatic induction, thereby enhancing overall TENG performance. In addition, TENG devices with varying active areas, ranging from 2 cm × 2 cm to 3 cm × 3 cm (Fig. 4c and d), were prepared to examine size-dependent behavior. Increasing the active area enhances the effective contact surface, leading to greater surface charge accumulation and stronger electrostatic induction, thereby increasing TENG voltage and current output. Such assessments are essential for validating scalability and ensuring stable performance.

By monitoring the output of PCL/Al TENG across a resistance range from kΩ to GΩ, the impact of the external load resistance on its electrical behavior was systematically investigated. Evaluating load-dependent performance is essential because efficient energy transfer in practical systems requires proper impedance matching between the TENG and connected electronic components. The output voltage and calculated power as a function of applied external resistance are shown in Fig. 5a and b. The power at various load resistances is calculated using the formula $P = V^2/R$, where V is the voltage, and R is the resistance. The highest power of 24.5 μW was recorded at a load resistance of 200 MΩ, corresponding to the

Open Access Article. Published on 14 May 2026. Downloaded on 6/5/2026 3:58:04 AM.
This article is licensed under a Creative Commons Attribution 3.0 Unported Licence.

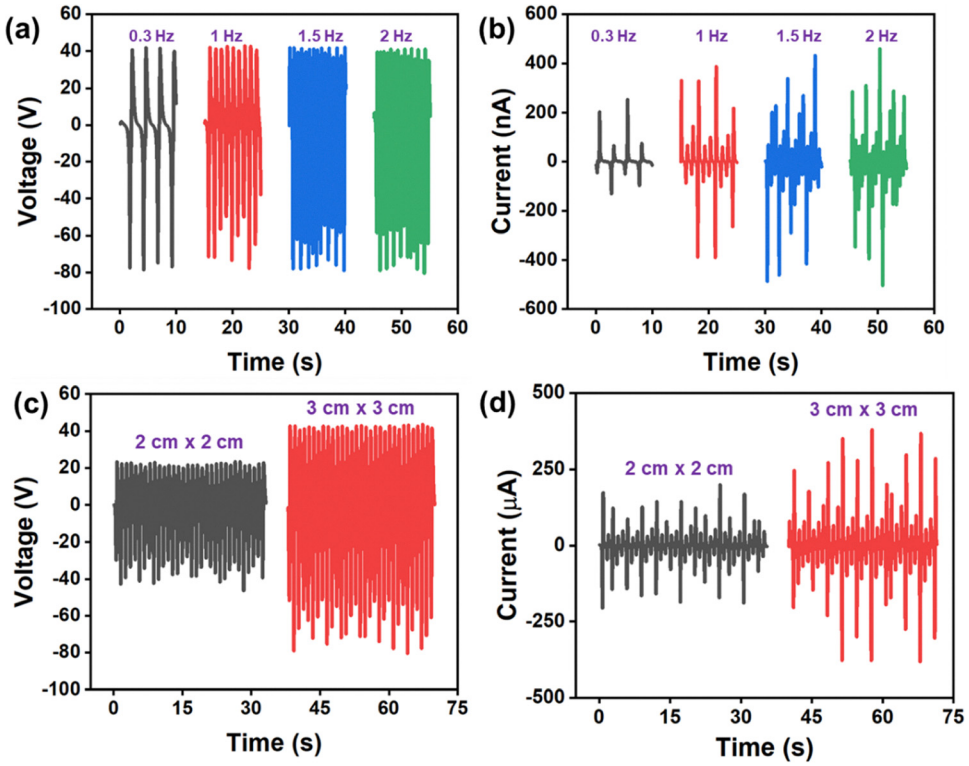

Fig. 4 (a) Output voltage of the PLA/Al TENG measured at different operating frequencies (0.3, 1, 1.5, and 2 Hz), (b) corresponding current responses of PLA/Al TENG under varying excitation frequencies, (c) output voltage signals obtained from devices with different active areas (2 cm × 2 cm and 3 cm × 3 cm), (d) corresponding current outputs of PLA/Al TENG for different device areas.

internal impedance of the proposed PCL/Al-based TENG. Fig. 5c shows the charging of capacitors using TENG from 1 to 10 μF, and the corresponding stored charges are shown in Fig. 5d. The alternating output from the PCL/Al TENG was first converted to direct current using a rectifier and subsequently stored in a conventional capacitor, which was then utilized to power small, portable electronic devices. The stored charge in the capacitor (Q) is given by $Q = CV$, where C is the capacitance, and V is the voltage.

To assess the robustness of TENG, its output voltage was continuously monitored for approximately 3 days, encompassing multiple mechanical actuation cycles, under an applied force of 5 N at 1 Hz (Fig. 6a). The voltage profile remained stable throughout the test, demonstrating excellent mechanical durability and reliable long-term energy-harvesting capability. The energy accumulated in a 2.2 μF capacitor was subsequently used to operate a small electronic calculator, as illustrated in Fig. 6b. The corresponding charge–discharge profiles of the capacitor during power to these devices are also presented. These findings demonstrate that the developed TENG can effectively function as a self-sustaining power source for low-power portable electronics. Fig. 6c shows the digital image of powering a calculator using the PCL/Al TENG. To validate the practical applicability of TENGs, the PCL/Al TENG was evaluated under real-world conditions by capturing the biomechanical energy generated from routine human activities. The corresponding voltage and current outputs recorded during these motions are presented in Fig. 6d–f. The device effectively converted mechanical forces generated during finger, palm tapping, and punching motions into electrical energy. During the motions, low-vibration mechanical energy is converted into electrical signals, demonstrating its potential for wearable energy-harvesting applications.

Conventional systems can record surface contacts and finger motions, but accurately identifying texture remains technically challenging. Contrast-based feature extraction and picture acquisition are commonly used in optical-based methods. Nevertheless, these techniques are highly susceptible to environmental changes, surface reflectivity, and lighting conditions. Additionally, they require heavy imaging equipment, which limits portability and real-time flexibility, especially when differentiating surfaces with minute roughness differences. Incorporating tactile sensing based on TENG into a robotic gripper offers a small, self-powered, and extremely sensitive substitute. Contact-induced mechanical stimuli, including friction, microvibrations, and pressure changes, are directly converted by TENG tactile sensors into electrical signals that naturally encode material texture. Fig. S4 shows the surface roughness texture of the various sandpapers taken into consideration using an optical microscope image. Fig. 7a shows the working and texture recognition capability of a TENG-integrated robotic gripper. The cyclic contact–separation process between the TENG and sandpaper surfaces, where full contact enables charge transfer and subsequent separation generates electrical signals.

 This journal is © The Royal Society of Chemistry and the Chinese Chemical Society 2026

Open Access Article. Published on 14 May 2026. Downloaded on 6/5/2026 3:58:04 AM.
This article is licensed under a Creative Commons Attribution 3.0 Unported Licence.

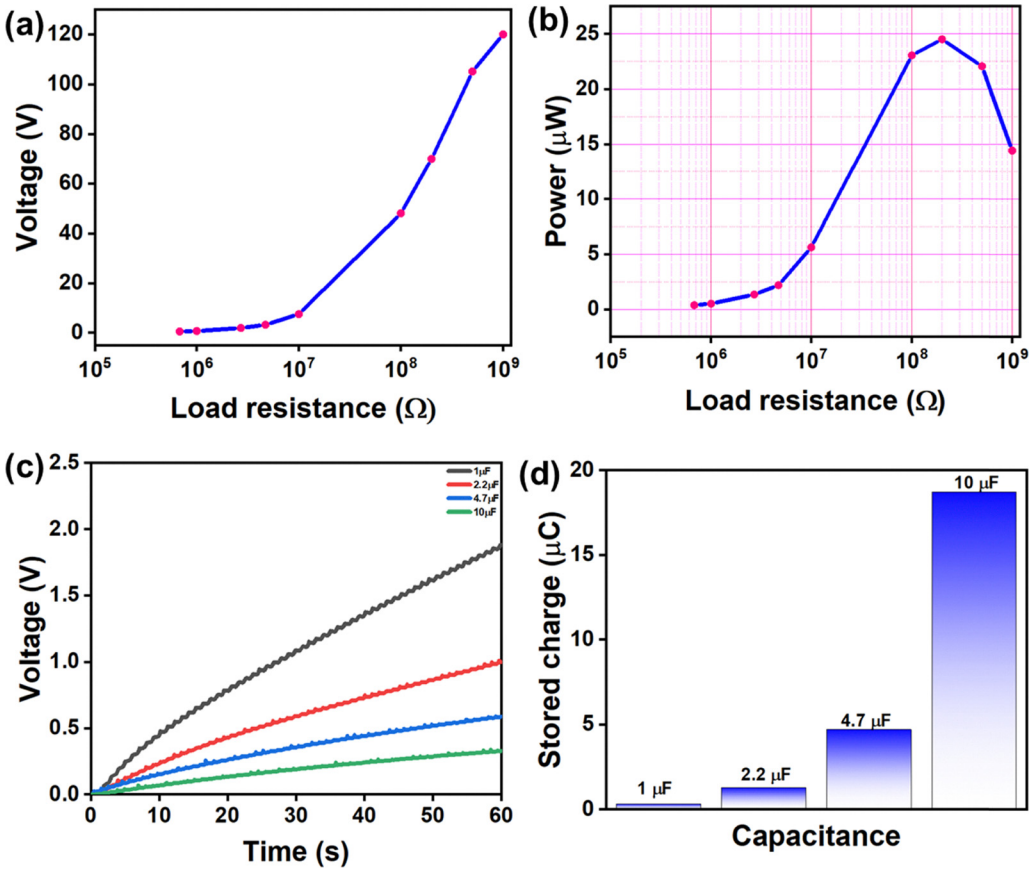

Fig. 5 (a) Output voltage of the PLA/Al TENG as a function of external load resistances, (b) corresponding output power *versus* load resistance, indicating the maximum power output at the optimal load resistance, (c) charging profiles of capacitors with different capacitances (1, 2.2, 4.7, and 10 μF), (d) stored charge measured for capacitors with varying capacitances.

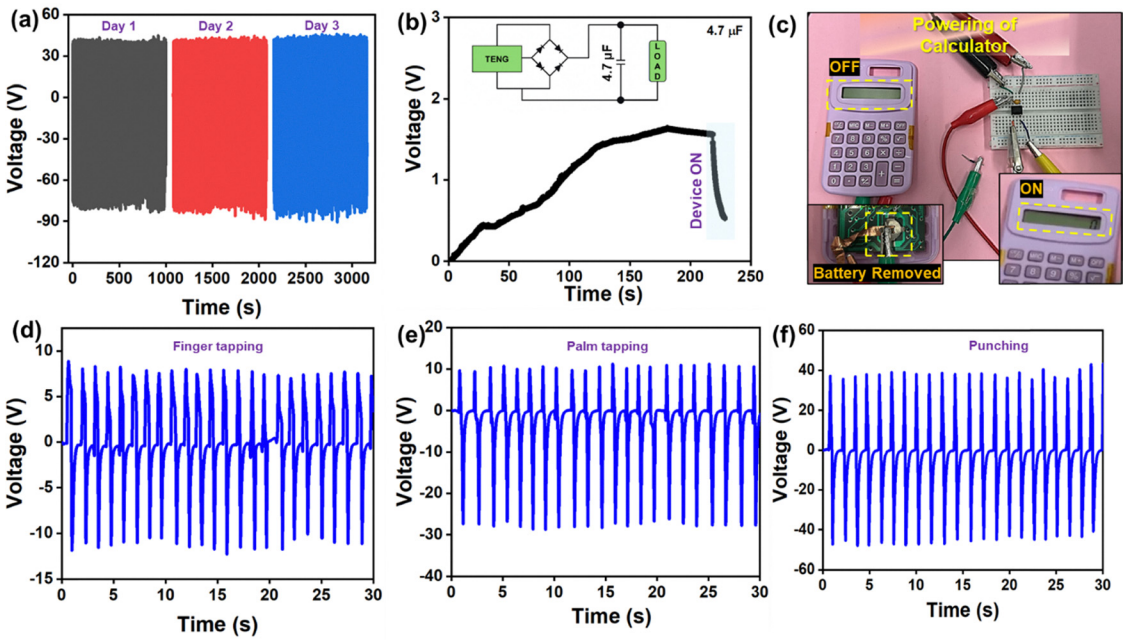

Fig. 6 (a) Long-term operational stability of the PLA/Al TENG measured over three consecutive days, demonstrating consistent voltage output, (b) charging behavior of a 4.7 μF capacitor through a rectifier circuit and by hand tapping upon the TENG, (c) photographic demonstration of the TENG powering a commercial calculator, (d)–(f) output voltage signals generated under different human mechanical stimuli, including finger tapping, palm tapping, and punching.

Open Access Article. Published on 14 May 2026. Downloaded on 6/5/2026 3:58:04 AM.
This article is licensed under a Creative Commons Attribution 3.0 Unported Licence.

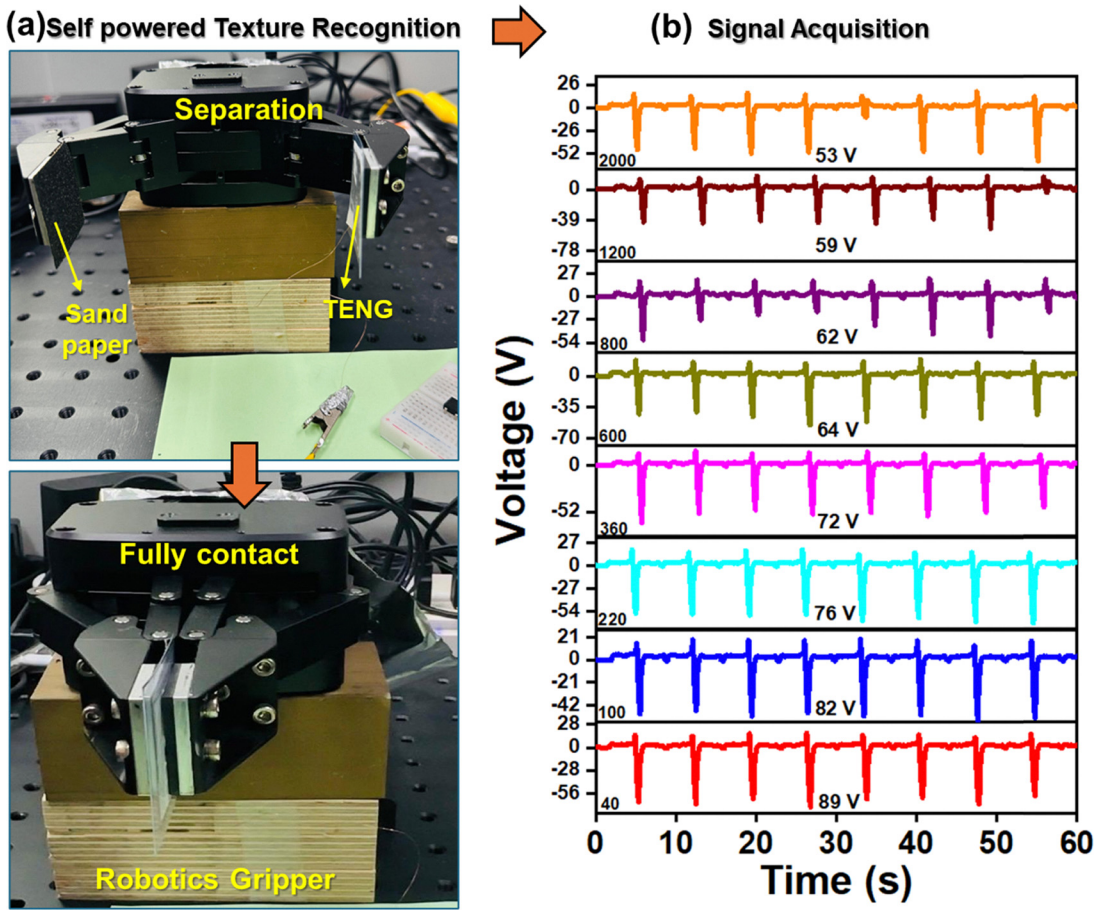

Fig. 7 (a) Photographic images of the robotic gripper-based experimental setup demonstrating the contact–separation operation of the TENG and (b) output voltage signals of the TENG recorded under varying sandpaper texture.

Fig. 7b presents time-dependent voltage outputs for different sandpaper grit sizes (40–2000), demonstrating that surface roughness significantly influences waveform characteristics. Overall, the results validate the TENG-based system as a self-powered tactile sensor capable of real-time texture recognition for robotic gripping applications.

Neural network methods provide an effective framework for material texture recognition. A dataset of 800 TENG sensor signal samples, 100 samples per class, representing eight different material classes (excitation conditions: 40, 100, 220, 360, 600, 800, 1200, and 2000) was used for the CNN-based material classification. Grey-scale images were created from the raw sensor inputs. Stratified random sampling was used to divide the dataset into 480 training, 160 validation, and 160 testing samples. The CNN architecture comprised three convolutional blocks, ReLU activation, max pooling, two fully connected layers, and an eight-neuron softmax output layer. The Adam optimizer was used to train the network. The hybrid feature extraction method used frequency-domain features (long-term spectral features) and time-domain patterns (short-term temporal dependencies) present in TENG signals, which were automatically discovered by hierarchical convolutional layers.

A hybrid feature-extraction approach enhances classification performance because TENG signals contain both time- and frequency-domain features, including short- and long-term dependencies. The confusion matrices for the training and validation datasets, obtained using the suggested CNN model for material classification, are shown in Fig. 8a and b, respectively. The columns represent the anticipated class labels, and the genuine class labels are represented by the rows. A unique excitation or material texture condition (40, 100, 220, 360, 600, 800, 1200, and 2000) is linked to each class. Strong diagonal dominance is observed in the confusion matrices for the training and validation datasets, indicating accurate classification across all eight classes. On both the training and validation sets, the CNN's accuracies were 96.9% and 91.9%, respectively. The few misclassifications found are mostly between closely related classes, demonstrating the model's strong generalization capabilities and efficient feature learning. Training and validation accuracies and training and validation losses over 20 training epochs are shown in Fig. 8c and d, respectively. The CNN model's successful convergence, effective learning of discriminative features, and robust generalization across the training and validation datasets are all confirmed by the accuracy and loss plots. These findings confirm that the

 This journal is © The Royal Society of Chemistry and the Chinese Chemical Society 2026

Open Access Article. Published on 14 May 2026. Downloaded on 6/5/2026 3:58:04 AM.
This article is licensed under a Creative Commons Attribution 3.0 Unported Licence.

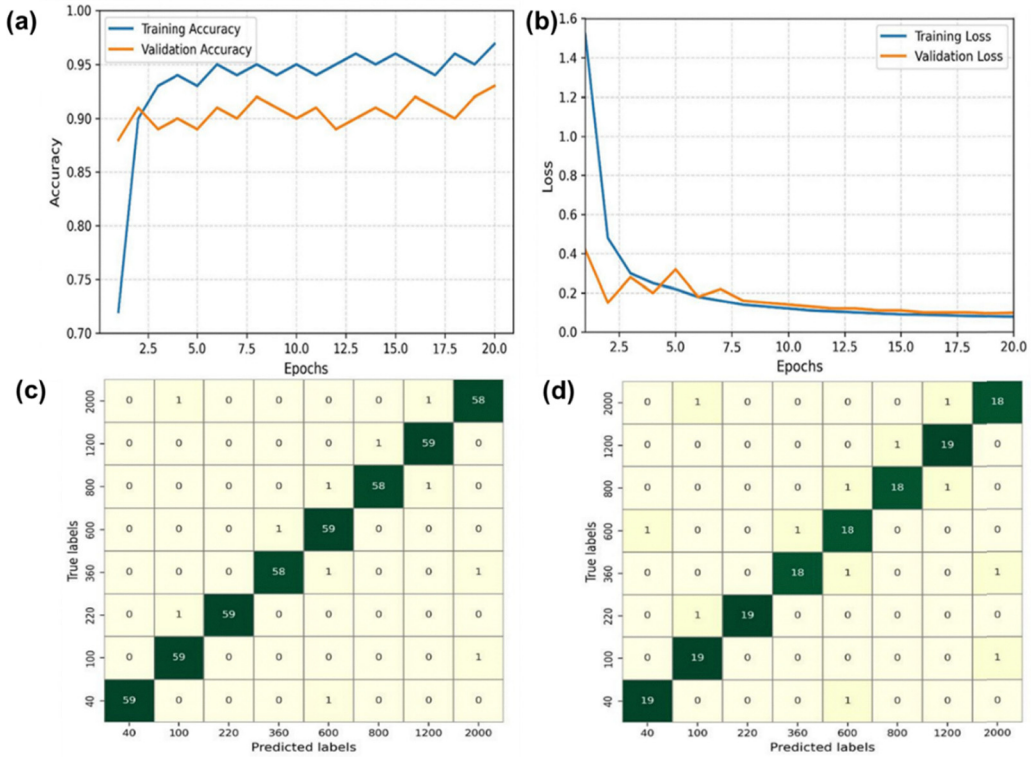

Fig. 8 Performance evaluation and classification results of the CNN model for surface texture recognition. (a) Training and validation accuracy over 20 training epochs, demonstrating model convergence, (b) training and validation loss curves over 20 epochs, and (c) and (d) confusion matrices for the (c) training and (d) validation datasets, showing the classification performance across eight distinct sandpaper grit sizes (40–2000).

CNN architecture is appropriate for precise material texture categorization utilizing TENG sensor data.

4. Conclusions

Escalating energy demand and environmental concerns have intensified the search for sustainable energy-generation technologies, positioning TENGs as promising candidates. Extending the triboelectric series with efficient biodegradable materials not only enhances material selection flexibility and device performance but also enables easy degradation at end-of-life, thereby significantly reducing long-term carbon footprint and waste accumulation. Biodegradable negative triboelectric layers, PLA, PCL, and PTMC, were combined with an opposite freely moving tribopositive aluminium layer; the TENG based on PCL/Al delivered an electrical output of 118 V and 772 nA. The higher electrical output of the PCL/Al TENG is attributed to the PCL layer's higher surface roughness and higher dielectric constant compared to other triboelectric layers, such as PLA and PTMC. Moreover, the system demonstrated applicability to human–motion-based energy harvesting and powering a calculator using TENG-generated energy.

Further, the single-electrode TENG was connected to the robotic gripper to trace various signals from different sandpaper surface textures. Then, the electrical output was incorporated into a convolutional neural network, which achieved accuracies of 96.9% and 91.9% on the training and validation sets, respectively. The proposed system enables intelligent perception and shows strong promise for real-time surface texture identification applications. In industrial automation, self-powered sensors based on TENG can be used for robotic manipulation tasks, including item identification, texture classification, and adaptive grasping. They are also promising for applications in prosthetics and human–machine interfaces that require tactile feedback. They may also be used in autonomous systems for real-time sensing without the need for external power sources, thereby improving energy efficiency and mobility. Overall, this study introduces a sustainable approach for engineering biodegradable negative triboelectric materials and advancing eco-friendly robotic TENG technologies.

Author contributions

Sugato Hajra: conceptualization, writing – original draft, investigation; Shibam Pal: writing – original draft, investigation; Kushal Ruthvik Kaja: investigation; Yoobin Choi: investigation; Swati Panda: visualization, data curation; Basanta Kumar Panigrahi: software; Hoe Joon Kim: funding acquisition, project administration, supervision, writing – review & editing; Anna Finne Wistrand: project administration, supervision, writing – review & editing.

Conflicts of interest

There are no conflicts to declare.

Open Access Article. Published on 14 May 2026. Downloaded on 6/5/2026 3:58:04 AM. This article is licensed under a Creative Commons Attribution 3.0 Unported Licence.

Data availability

The data supporting the findings of this study are available from the corresponding author upon reasonable request. All relevant data generated or analysed during this study are included in this article.

Supplementary information (SI) is available. See DOI: https://doi.org/10.1039/d6qm00202a.

Acknowledgements

This work was supported by the National Research Foundation of Korea (NRF) grant funded by the Ministry of Science and ICT (MSIT) (No. RS-2024-00346135, RS-2024-00406674) and the Ministry of Education (No. RS-2025-25420118).

References

1 J. A. E. Hughes, P. Maiolino and F. Iida, An Anthropomorphic Soft Skeleton Hand Exploiting Conditional Models for Piano Playing, *Sci. Robot.*, 2018, **3**, eaau3098.
2 S. Asif, M. Bueno, P. Ferreira, P. Anandan, Z. Zhang, Y. Yao, G. Ragunathan, L. Tinkler, M. Sotoodeh-Bahraini, N. Lohse, P. Webb, W. Hutabarat and A. Tiwari, Rapid and automated configuration of robot manufacturing cells, *Robot. Comput. Integr. Manuf.*, 2025, **92**, 102862.
3 X. Fu, Y. Chen, S. Xie, M. Cao, Q. Zhao, Y. Liu, Y. Li, S. Wang, X. Cheng and L. Xie, All-screen-printed tactile sensor for robotic arm via polymeric thermal foaming, *Chem. Eng. J.*, 2025, **519**, 165542.
4 X. Zhang, L. Wu, S. He, Z. Sha, Y. Huang, S. Wu, D. Chu, C. H. Wang and S. Peng, Recent Advances of Slip Sensors for Smart Robotics, *Adv. Mater. Technol.*, 2026, e02251.
5 J. Guo, L. Zhao, Z. Ouyang, Q. Zuo, Y. Liang and J. Leng, All-in-One Soft Capacitive Pressure Sensor with Adaptive Self-Healing Property in Diverse Harsh Environments, *Adv. Funct. Mater.*, 2026, **36**, e25419.
6 C. M. Costa, V. F. Cardoso, P. Martins, D. M. Correia, R. Gonçalves, P. Costa, V. Correia, C. Ribeiro, M. M. Fernandes, P. M. Martins and S. Lanceros-Méndez, Smart and Multifunctional Materials Based on Electroactive Poly(vinylidene fluoride): Recent Advances and Opportunities in Sensors, Actuators, Energy, Environmental, and Biomedical Applications, *Chem. Rev.*, 2023, **123**, 11392–11487.
7 W. Tang, Q. Sun and Z. L. Wang, Self-powered sensing in wearable electronics—a paradigm shift technology, *Chem. Rev.*, 2023, **123**, 12105–12134.
8 L. Gao, K. Liu, W. Wang, X. Li, Q. Deng, N. Hu, X. Chen and X. Mu, Intelligent Soft Robotic System for Sensing and Recognition via Triboelectric-Based Multi-Sensor Fusion, *Adv. Funct. Mater.*, 2026, **36**, e17158.
9 Y. Qiu, F. Wang, Z. Zhang, K. Shi, Y. Song, J. Lu, M. Xu, M. Qian, W. Zhang, J. Wu, Z. Zhang, H. Chai, A. Liu, H. Jiang and H. Wu, Quantitative softness and texture bimodal haptic sensors for robotic clinical feature identification and intelligent picking, *Sci. Adv.*, 2024, **10**, eadp0348.
10 S. Hajra, S. Panda, H. Khanberh, V. Vivekananthan, E. Chamanehpour, Y. K. Mishra and H. J. Kim, Revolutionizing self-powered robotic systems with triboelectric nanogenerators, *Nano Energy*, 2023, **115**, 108729.
11 W. Sun, B. Li, F. Zhang, C. Fang, Y. Lu, X. Gao, C. Cao, G. Chen, C. Zhang and Z. L. Wang, TENG-Bot: Triboelectric nanogenerator powered soft robot made of uni-directional dielectric elastomer, *Nano Energy*, 2021, **85**, 106012.
12 G. Yao, L. Xu, X. Cheng, Y. Li, X. Huang, W. Guo, S. Liu, Z. L. Wang and H. Wu, Bioinspired Triboelectric Nanogenerators as Self-Powered Electronic Skin for Robotic Tactile Sensing, *Adv. Funct. Mater.*, 2020, **30**, 1907312.
13 S. Hajra, S. Panda, S. Song, B. K. Panigrahi, P. Pakawanit, S. M. Jeong and H. J. Kim, Flexible composite material for self-powered applications via triboelectricity and mechanoluminescence: PDMS/ZnS: Cu composites, *Nano Energy*, 2023, **114**, 108668.
14 A. Babu and D. Mandal, Roadmap to Human–Machine Interaction through Triboelectric Nanogenerator and Machine Learning Convergence, *ACS Appl. Energy Mater.*, 2024, **7**, 822–833.
15 S. Panda, S. Hajra, Y. Oh, W. Oh, J. Lee, H. Shin, V. Vivekananthan, Y. Yang, Y. K. Mishra and H. J. Kim, Hybrid nanogenerators for ocean energy harvesting: mechanisms, designs, and applications, *Small*, 2023, **19**, 2300847.
16 P. S. Bhosale, S. Panda, D. Ramu, S. Hajra, K. R. Kaja, M. Belal, E. Kim and H. J. Kim, Triboelectric nanogenerators for smart industrial sensing applications, *Adv. Ind. Eng. Chem.*, 2025, **1**, 40.
17 Q. Zhang, C. Xin, F. Shen, Y. Gong, Y. Zi, H. Guo, Z. Li, Y. Peng, Q. Zhang and Z. L. Wang, Human body IoT systems based on the triboelectrification effect: energy harvesting, sensing, interfacing and communication, *Energy Environ. Sci.*, 2022, **15**, 3688–3721.
18 C. Jiang, X. Li, Y. Ying and J. Ping, A multifunctional TENG yarn integrated into agrotextile for building intelligent agriculture, *Nano Energy*, 2020, **74**, 104863.
19 T. Sun, C. Yao, Z. Liu, S. Huang, X. Huang, S. Zheng, J. Liu, P. Shi, T. Zhang and H. Chen, Machine learning-coupled vertical graphene triboelectric pressure sensors array as artificial tactile receptor for finger action recognition, *Nano Energy*, 2024, **123**, 109395.
20 S. Hao, J. Jiao, Y. Chen, Z. L. Wang and X. Cao, Natural wood-based triboelectric nanogenerator as self-powered sensing for smart homes and floors, *Nano Energy*, 2020, **75**, 104957.
21 S. Hajra, K. R. Kaja, S. Panda, S. Song, S. M. Jeong, Y. K. Mishra, T. H. Oh, G. Das, S. Divya and H. J. Kim, Mechanoluminescence: Mechanisms, emerging applications, and future prospects, *Nano Energy*, 2025, **145**, 111418.
22 D. W. Kim, J. H. Lee, J. K. Kim and U. Jeong, Material aspects of triboelectric energy generation and sensors, NPG Asia, *Materials*, 2020, **12**, 6.
23 J. Zhu, H. Yang, L. Cao, C. Dai, J. Ren, J. Liang and S. Ling, Functionalization of structural materials through electro-blown spinning of ultrathin and transparent silk fibroin ionotronic nanofiber skin, *Nano Today*, 2023, **50**, 101873.

 This journal is © The Royal Society of Chemistry and the Chinese Chemical Society 2026

Open Access Article. Published on 14 May 2026. Downloaded on 6/5/2026 3:58:04 AM.
This article is licensed under a Creative Commons Attribution 3.0 Unported Licence.

24 D. Nitzan, Development of intelligent robots: achievements and issues, *IEEE Trans. Robot. Automat.*, 2003, **1**, 3–13.
25 T. Jin, Z. Sun, L. Li, Q. Zhang, M. Zhu, Z. Zhang, G. Yuan, T. Chen, Y. Tian, X. Hou and C. Lee, Triboelectric nanogenerator sensors for soft robotics aiming at digital twin applications, *Nat. Commun.*, 2020, **11**, 5381.
26 B. Shi, Z. Liu, Q. Zheng, J. Meng, H. Ouyang, Y. Zou, D. Jiang, X. Qu, M. Yu and L. Zhao, Body-Integrated Self-Powered System for Wearable and Implantable Applications, *ACS Nano*, 2019, **13**, 6017–6024.
27 Y. Zhou, M. Shen, X. Cui, Y. Shao, L. Li and Y. Zhang, Triboelectric nanogenerator based self-powered sensor for artificial intelligence, *Nano Energy*, 2021, **84**, 105887.
28 Z. L. Wang, From contact electrification to triboelectric nanogenerators, *Rep. Prog. Phys.*, 2021, **84**, 096502.
29 X. Peng, K. Dong, C. Ning, R. Cheng, J. Yi, Y. Zhang, F. Sheng, Z. Wu and Z. L. Wang, All-nanofiber self-powered skin-interfaced real-time respiratory monitoring system for obstructive sleep apnea-hypopnea syndrome diagnosing, *Adv. Funct. Mater.*, 2021, **31**, 2103559.
30 L. Yan, Y. Mi, Y. Lu, Q. Qin, X. Wang, J. Meng, F. Liu, N. Wang and X. Cao, Weaved piezoresistive triboelectric nanogenerator for human motion monitoring and gesture recognition, *Nano Energy*, 2022, **96**, 107135.
31 C. Pei, H. Zhang, Y. Li, Z. Gu, X. Chen and T. Kuang, Robust and durable biodegradable polymer-based triboelectric nanogenerators enabled by trace amounts of melanin-like nanoparticles, *Nano Energy*, 2025, **135**, 110643.
32 H.-J. Kan, C.-H. Chi, J.-W. Han, H. Yang, S.-C. Lai, P.-H. Chen, P.-L. Liu and R.-H. Lee, Enhanced Triboelectric Nanogenerator Performance Using Cellulose Nanocrystal-Incorporated Electrospun PVDF-HFP Nanofibrous Membranes, *ACS Appl. Energy Mater.*, 2025, **8**, 17530–17543.
33 E. S. Hosseini, S. Dervin, P. Ganguly and R. Dahiya, Biodegradable materials for sustainable health monitoring devices, *ACS Appl. Bio Mater.*, 2021, **4**, 163–194.
34 H. Afshar, F. Kamran and F. Shahi, Recent progress in energy harvesting technologies for self-powered wearable devices: the significance of polymers, *Polym. Adv. Technol.*, 2025, **36**, e70187.
35 A. Chen, C. Zhang, G. Zhu and Z. L. Wang, Polymer materials for high-performance triboelectric Nanogenerators, *Adv. Sci.*, 2020, **7**, 2000186.
36 C. Wu, T. W. Kima, S. Sung, J. H. Park and F. Li, Ultrasoft and cuttable paper-based triboelectric nanogenerators for mechanical energy harvesting, *Nano Energy*, 2018, **44**, 279–287.
37 Y.-T. Jao, P.-K. Yang, C.-M. Chiu, Y.-J. Lin, S.-W. Chen, D. Choi and Z.-H. Lin, A textile-based triboelectric nanogenerator with humidity-resistant output characteristic and its applications in self-powered healthcare sensors, *Nano Energy*, 2018, **50**, 513–520.
38 Y. Guo, X.-S. Zhang, Y. Wang, W. Gong, Q. Zhang, H. Wang and J. Brugger, All-fiber hybrid piezoelectric-enhanced triboelectric nanogenerator for wearable gesture monitoring, *Nano Energy*, 2018, **48**, 152–160.
39 A. Takagi, Y.-I. Hsu and H. Uyama, Biodegradable poly (lactic acid) and polycaprolactone alternating multiblock copolymers with controllable mechanical properties, *Polym. Degrad. Stab.*, 2023, **218**, 110564.